MATERIALS CHEMISTRY FRONTIERS

RESEARCH ARTICLE

View Article Online
View Journal | View Issue

Cite this: *Mater. Chem. Front.*, 2021, **5**, 6618

In/ZnO@C hollow nanocubes for efficient electrochemical reduction of CO_2 to formate and rechargeable Zn–CO_2 batteries†

Xue Teng,[a] Yanli Niu,[a] Shuaiqi Gong,[a] Mingze Xu,[a] Xuan Liu,[a] Lvlv Ji[b] and Zuofeng Chen*[a]

Indium (In)-based materials are considered promising electrocatalysts for CO_2 reduction to formic acid, but their performance is usually limited by low current density and poor stability. Here, we describe In/ZnO@C hollow nanocubes (NCs), derived from $In(OH)_3$-doped Zn-MOF (*i.e.* ZIF-8) solid nanocubes, as high-performance CO_2-reduction electrocatalysts. The unique nanocube morphology of Zn-MOF makes it an ideal matrix for dispersing $In(OH)_3$ which can avoid aggregation. The formation of a hollow structure is associated with metallic In formation and CO_2/CO gas release, resulting from the carbothermal reduction reaction between $In(OH)_3$ and the carbon matrix. In/ZnO@C NCs exhibit excellent catalytic activity and selectivity for formate production, reaching a partial current density of 23.5 mA cm^{-2} with a Faradaic efficiency of 90% at −1.2 V *vs.* RHE in 0.5 M aqueous $KHCO_3$ solutions, which is greatly superior to In-free ZnO@C NCs and simple In nanoparticles. Solar-driven electrochemical CO_2/H_2O splitting can be realized by coupling the In/ZnO@C cathode with a RuO_2 anode, offering a promising route to the storage of renewable energy. As a promising technique for CO_2 fixation/utilization and energy conversion/storage, an aqueous rechargeable Zn–CO_2 battery with In/ZnO@C as the cathode is also constructed. It can output electrical energy with an open-circuit voltage of 1.35 V and a peak power density of 1.32 mW cm^{-2} while simultaneously realizing CO_2 conversion to formate. The Zn–CO_2 battery with In/ZnO@C inspires the development of green energy conversion and storage systems combining eco-efficient CO_2 utilization.

Received 5th June 2021,
Accepted 14th July 2021

DOI: 10.1039/d1qm00825k

rsc.li/frontiers-materials

Introduction

The electrochemical CO_2 reduction reaction (CO_2RR) is a potentially efficacious strategy for tackling global energy concerns, in particular, closing the carbon cycle, and the storage of renewable electrical energy from chemicals or fuels.[1] The past few decades have witnessed the discovery and development of various efficient electrocatalysts, which have led to a diversity of products with different selectivities.[2,3] CO_2 can be reduced to various value-added chemicals, including C_1 (CO, HCOOH, CH_4, *etc.*), C_2 (C_2H_4, CH_3COOH, *etc.*), and C_3 (*n*-propanol) products through different electrocatalytic reduction pathways.[4,5] To be feasible and competitive, the reactions must achieve a high conversion efficiency and selectivity. Formic acid, widely used in the tanning industry and fuel cells, is an ideal CO_2-conversion product owing to its high energy density and easy separation from the unreacted CO_2 gas stream ($CO_2 + 2H^+ + 2e^- \rightarrow HCOOH$, −0.19 V *vs.* the reversible hydrogen electrode, RHE).[6,7] In fact, CO_2 reduction to formic acid is highly desirable due to its high market and economic value and the relatively low energy input needed.[8] However, driving CO_2RR is challenging because of the thermodynamic stability of CO_2 (C═O, 806 kJ mol^{-1}) and competition from the hydrogen evolution reaction (HER) in aqueous media.[7,9]

Previous studies have identified several transition and post-transition metals, including Cd, Hg, In, Sn, Tl, Pb, and Bi, as selective electrocatalysts for CO_2 reduction to formate.[10–13] Among them, In has been suggested as a promising catalyst for practical formate production since it is less toxic and more environmentally benign than many of its neighbours.[8] Recent research studies have shown that In-based electrocatalysts can reduce CO_2 to formate in an aqueous electrolyte with satisfactory Faradaic efficiency (FE) values, but their performance is usually limited by a low current density and poor stability. For example, the oxidized In foil was found to reduce CO_2 to formate with a high selectivity of >90%, but the current density was lower than

[a] *School of Chemical Science and Engineering, Tongji University, 1239 Siping Road, Shanghai 200092, China. E-mail: zfchen@tongji.edu.cn*
[b] *School of Materials Science and Engineering, Zhejiang Sci-Tech University, Hangzhou 310018, China*

† Electronic supplementary information (ESI) available. See DOI: 10.1039/d1qm00825k

10 mA cm^{-2} at a potential of −1.3 V *vs.* RHE for achieving the formate FE.[14] Even on a gas-diffusion In/carbon electrode, the total current density reached only 6.2 mA cm^{-2} at −1.2 V.[15] Thus, the performance of In-based catalysts, in terms of activity and stability, needs to be further promoted prior to practical applications. However, the construction of advanced In-based catalysts or corresponding precursors is usually restricted by the limited coordination capability of In ions, which are essential for building blocks in functional materials such as metal–organic frameworks (MOFs).

MOFs can be constructed from designable building blocks to impart unique properties for a wide range of potential applications including gas adsorption, separation, sensing, and catalysis.[16–18] Furthermore, MOFs have been widely employed as sacrificial templates to form functional materials of porous structures.[19–21] Manipulating the morphology of catalysts to create a nanosized porous structure has recently been recognized as an effective means of enhancing the catalytic performance.[12,15,22–24] In particular, hollow nanostructures, as an intensive focus of research on energy-related applications, can provide more exposed active sites and shorten transport lengths for both ions and charges, as compared with corresponding architectures with solid interiors.[25–27] In this aspect, Zn-based electrocatalysts derived from Zn-MOFs represent one of the promising non-noble-metal catalysts for CO_2RR, but these materials usually lead to the CO product. Adding a second metal to Zn-based materials is potentially an effective approach for tuning the activity and selectivity through tailoring the binding strength and/or binding configuration of intermediates on the catalytic surfaces, while maintaining the morphology and structure advantages of Zn-based materials.[28,29]

Metal–CO_2 batteries with CO_2 as the cathode-active species give rise to opportunities to deal with energy and environmental issues simultaneously. This technology can transform waste CO_2 to value-added chemicals and fuels, reserve surplus electricity from renewable power, and balance the electricity supply and carbon cycle.[30] Inspired by aqueous metal–air batteries,[31,32] designing metal–CO_2 batteries that work in aqueous electrolytes, such as aqueous Zn–CO_2 batteries, can be an alternative for eco-efficient CO_2 utilization in practical applications. Aqueous Zn–CO_2 batteries implement flexible CO_2 electrochemistry for producing value-added products accompanied by energy storage based on a proton-coupled electron-transfer mechanism.

In this study, we describe an In/ZnO@C hollow nanocube electrocatalyst derived from $In(OH)_3$-doped Zn-MOF (*i.e.* ZIF-8) precursors. The *in situ* doping of $In(OH)_3$ and the unique nanocube morphology of Zn-MOFs are beneficial for avoiding aggregation. The formation of the hollow structure is associated with metallic In formation and CO_2/CO gas release, resulting from the carbothermal reduction reaction between $In(OH)_3$ and the carbon matrix. The activity and selectivity of In/ZnO@C for CO_2 reduction to formate are notable, reaching a partial current density of 23.5 mA cm^{-2} with a FE of ∼90% for formate production at −1.2 V (*vs.* RHE). Inspired by the excellent CO_2RR performance, we further constructed a full cell for CO_2/H_2O splitting by coupling the In/ZnO@C cathode with a RuO_2 anode. A long-term test was conducted at 2.7 V and the current density was sustained at around 8 mA cm^{-2} during the whole period. Furthermore, an aqueous rechargeable Zn–CO_2 battery was constructed using the In/ZnO@C cathode, which could deliver a peak power density of 1.32 mW cm^{-2} during the discharge process and be cycled by discharging–charging at 1 mA cm^{-2} over 51 h (153 cycles), realizing the utilization of CO_2 and electrical energy output. The Zn–CO_2 battery with In/ZnO@C sets up a fascinating platform for the rational utilization of CO_2RR electrocatalysts in sustainable energy-conversion systems.

Results and discussion

Preparation and characterization of catalysts

The fabrication of In/ZnO@C hollow nanocubes (NCs) is illustrated in Scheme 1. The detailed procedures are provided in the ESI.† As the precursors, $In(OH)_3$-doped Zn-MOF nanocubes were first prepared by a co-precipitation method with 2-MeIM (2-methylimidazole), $In(NO_3)_3$, $Zn(NO_3)_2$ and CTAB under continuous stirring. The $In(OH)_3$–Zn-MOF precursors have a regular nanocube morphology with an average size of about 200 nm, as shown in the scanning electron microscopy (SEM) image in Fig. 1A. Moreover, the transmission electron microscopy (TEM) image reveals that these precursors have solid interiors (Fig. S1, ESI†). The X-ray diffraction (XRD) pattern exhibits diffraction peaks corresponding to $In(OH)_3$ and Zn-MOF (*i.e.* ZIF-8; deposition No. 602542)[33] (Fig. S2A, ESI†). The energy dispersive X-ray (EDX) spectrum confirms the existence of In, Zn, N, C and O elements in the precursors (Fig. S2B, ESI†).

The In/ZnO@C hollow nanocubes were obtained by annealing $In(OH)_3$–Zn-MOF solid nanocubes at 600 °C for 2 h in an Ar atmosphere. SEM images (Fig. 1B and C) show that the pyrolyzed product maintains the original nanocube morphology of the precursors, while the TEM image (Fig. 1D) reveals the formation of the hollow interior. The formation of the hollow structure is presumably associated with the carbothermal reduction reaction between $In(OH)_3$ and the carbon matrix, with the former converted to metallic In and the latter to CO_2/CO gas.[34] In the high-resolution TEM (HRTEM) image (Fig. 1E), lattice fringes are observed with interplanar spacing values of 0.27 nm for the (101) plane of In and 0.248 nm for the (101) plane of ZnO. The polycrystalline nature of the material was further confirmed by the selected area electron diffraction (SAED) pattern in the inset. The high-angle annular dark-field scanning TEM (HAADF-STEM) image and the corresponding elemental mapping (Fig. 1F) reveal the uniform distribution of In, Zn, C and N elements over the entire hollow nanocube. The porous and hollow structural characteristics may provide more exposed active sites for CO_2 reduction, as compared with the corresponding architecture with a solid interior.

For comparison, undoped Zn–MOF nanocubes (see the Experimental section in the ESI†) were also prepared as precursors (Scheme 1). SEM and TEM images (Fig. S3, ESI†) show that the Zn–MOF has the expected nanocube morphology. The XRD pattern and EDX spectrum (Fig. S4, ESI†) confirm the formation of the pure ZIF-8 MOF. Annealing Zn–MOF at 600 °C and 950 °C in an Ar atmosphere gives ZnO@C (Fig. 1G) and Zn-free carbon NCs (Fig. 1H), respectively. For the latter,

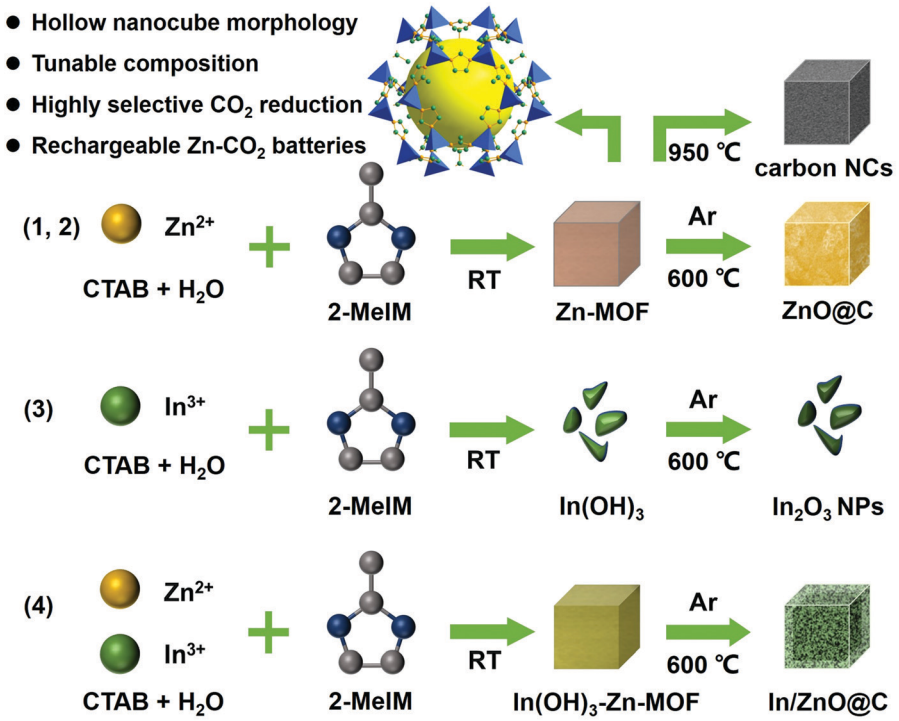

Scheme 1 Schematic illustration of the fabrication of carbon NCs, ZnO@C NCs, In_2O_3 NPs and In/ZnO@C NCs as CO_2RR electrocatalysts.

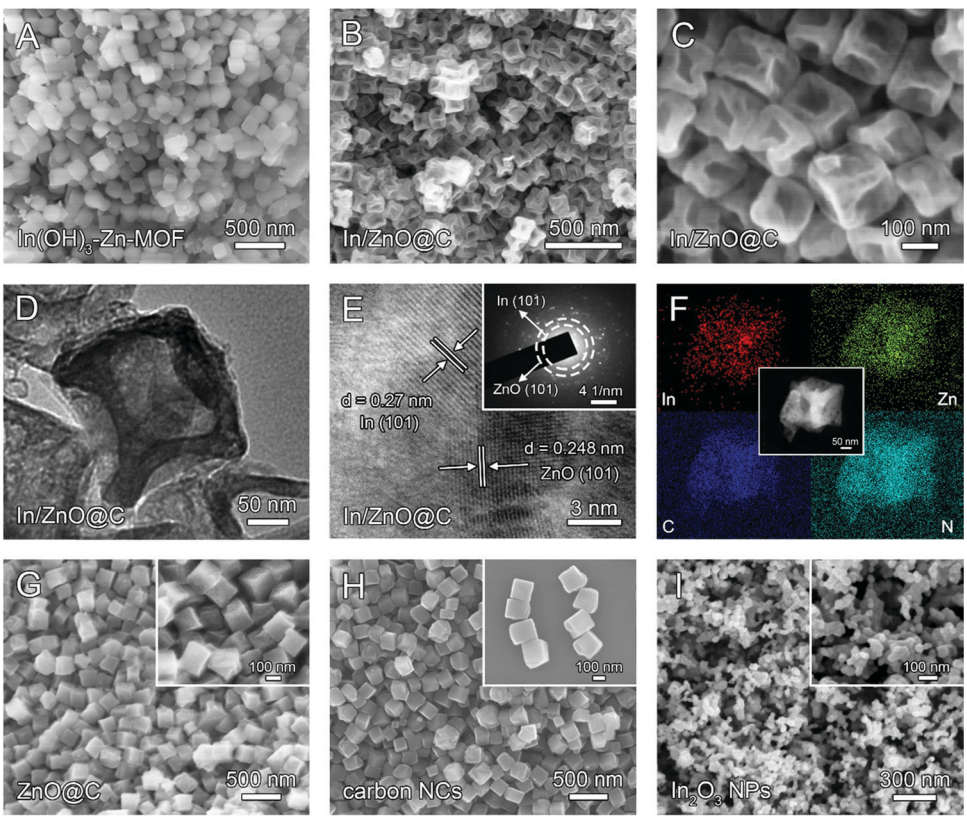

Fig. 1 SEM images of (A) $In(OH)_3$–Zn-MOF precursors and (B and C) In/ZnO@C. (D) TEM, (E) HRTEM (inset, SAED pattern), and (F) elemental mapping images of In/ZnO@C. SEM images of (G) ZnO@C, (H) carbon NCs and (I) In_2O_3 NPs.

pyrolysis at 950 °C is accompanied by evaporation of the Zn ions in the Zn–MOF precursor (the boiling point of Zn is 907 °C). Unlike In/ZnO@C with a hollow structure, the ZnO@C and carbon NCs have solid interiors, which is confirmed by the TEM images shown in Fig. S5 and S6 (ESI†), respectively.

In another control experiment without added Zn salts, only irregular $In(OH)_3$ nanoparticles were formed (Fig. S7 and S8, ESI†), which was consistent with the non-coordination between In ions and 2-MeIM. Additional evidence for involving no 2-MeIM in the precipitate is provided by the Fourier transform infrared (FT-IR) spectra (Fig. S9, ESI†) and thermogravimetric analysis (TGA) curves (Fig. S10, ESI†). Through calcination at 600 °C, $In(OH)_3$ NPs are converted to the corresponding In_2O_3 NPs, as shown in Fig. 1I.

Fig. 2A shows XRD patterns of the In/ZnO@C, ZnO@C, carbon NCs and In_2O_3 NPs. For In/ZnO@C, all diffraction peaks can be well indexed to metallic In (JCPDS No. 85-1409) and ZnO (JCPDS No. 36-1451). The strong peaks at 32.95°, 39.16°, 54.46° and 67.04° correspond to the crystal planes (101), (110), (112), and (211), respectively, in metallic In, while the peaks at 31.82°, 34.47°, 36.2°, 47.57° and 67.86° correspond to (100), (002), (101), (102) and (112), respectively, in ZnO. For ZnO@C, only characteristic peaks corresponding to ZnO are observed. By increasing the pyrolysis temperature from 600 °C to 950 °C, the resultant material, *i.e.* carbon NCs, exhibits no discernable peaks in the XRD pattern and the inexistence of the metallic element in EDX (Fig. S11, ESI†) because of the evaporation of Zn ions in the Zn–MOF precursor.[35] The XRD and EDX results (Fig. S12, ESI†) also confirm the formation of In_2O_3 NPs (JCPDS No. 44-1087).

The surface electronic states and chemical compositions of the as-prepared samples were further investigated by X-ray

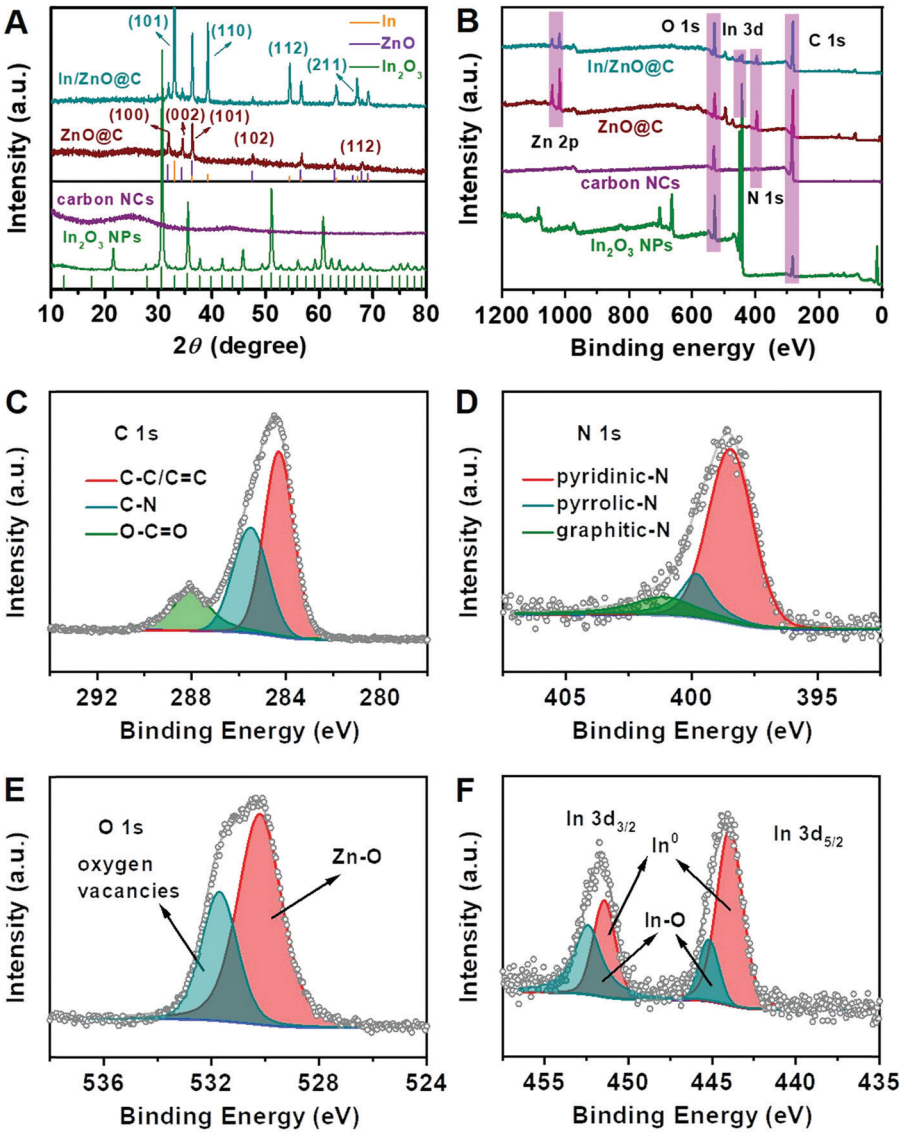

Fig. 2 (A) XRD patterns and (B) full XPS spectra of In/ZnO@C, ZnO@C, carbon NCs, and In_2O_3 NPs. High-resolution XPS spectra of (C) C 1s, (D) N 1s, (E) O 1s and (F) In 3d for In/ZnO@C.

photoelectron spectroscopy (XPS). The full survey XPS spectra of In/ZnO@C, ZnO@C, carbon NCs and In_2O_3 NPs are shown in Fig. 2B. While the other three samples exhibit the characteristic peaks of N 1s, the In_2O_3 NPs contain no N 1s signals, consistent with the non-coordination between In ions and 2-MeIM. For the high-resolution XPS, the C 1s spectrum (Fig. 2C) can be deconvoluted into three dominant peaks. Specifically, the main peak at around 284.3 eV corresponds to conjugated C–C/C=C bonds (sp^2 carbon), while the peaks at 285.5 and 288.1 eV correspond to different bonding structures of C–N and O–C=O, respectively.[36–38] For the high-resolution N 1s XPS of In/ZnO@C (Fig. 2D), three types of nitrogen can be identified after deconvolution, namely hexagonal pyridinic-N at 398.5 eV, pyrrolic-N at 399.8 eV, and graphitic-N at 401.2 eV.[31,39–41] The O 1s XPS shown in Fig. 2E is divided into two peaks. The peak at the binding energy of 530.2 eV is attributed to the bond of Zn–O,[42] and the other peak at 531.7 eV is assigned to O atoms in the vicinity of oxygen vacancies.[43] In Fig. 2F, the In 3d XPS spectrum can fitted well with two sets of peaks that correspond to metallic In and In_2O_3 species, respectively, with the latter arising from surface oxidation.[12,14] For comparison, the high-resolution XPS spectra of ZnO@C,[44] carbon NCs and In_2O_3 NPs are shown in Fig. S13–S15 (ESI†).

Raman spectra (Fig. S16, ESI†) can provide the extent of graphitization for In/ZnO@C, ZnO@C and carbon NCs. The typical G (1583 cm^{-1}) and D (1340 cm^{-1}) bands are attributed to hexagonally bonded carbon atoms inside the graphitic network and the distorted carbon structure on the defect sites, respectively.[45] The I_D/I_G ratio of In/ZnO@C (0.89) is lower than 1, indicating a higher degree of graphitization in the carbon layer, which is beneficial for electron transport.[41] For TGA curves under an air atmosphere (Fig. S17, ESI†), the two-step mass-loss behavior of the In/ZnO@C and ZnO@C samples is attributable to the amorphous and graphitized carbons, implying their carbon nature. By contrast, the In_2O_3 sample exhibits high thermal stability because of the involvement of no 2-MeIM and associated carbon species. The molar ratio of In and Zn in In/ZnO@C was determined to be 2 : 3 using inductively coupled plasma-optical emission spectrometry (ICP-OES) with the standard curves as shown in Fig. S18 (ESI†).

Electrochemical CO_2 reduction

The electrocatalytic CO_2RR performance of the as-prepared In/ZnO@C, ZnO@C and In_2O_3 NPs was evaluated using a gas-tight two-compartment H-cell with a three-electrode system in N_2- and CO_2-saturated 0.5 M $KHCO_3$. As illustrated in Fig. 3A, the current density of In/ZnO@C (26 mA cm^{-2} at −1.2 V *vs.* RHE) is higher than that of ZnO@C (19 mA cm^{-2}) and In_2O_3 NPs (6.7 mA cm^{-2}). The gaseous and liquid products are quantitatively analyzed *via* online gas chromatography (GC) (Fig. S19, ESI†) and ^1H nuclear magnetic resonance (^1H NMR) spectroscopy (Fig. S20, ESI†), respectively, after electrolysis for 2 hours. As shown in Fig. 3B, In/ZnO@C exhibits the highest FE_{HCOO^-} of 90% with a small FE_{CO} of 2% and a FE_{H_2} of 8% at a potential of −1.2 V *vs.* RHE. The FE_{HCOO^-} value is decreased by increasing the applied potential, which is accompanied with an increase in FE_{H_2}. This result can be at least partially attributed to the limited mass transport of CO_2 with a low concentration in aqueous solution.[46] By contrast, the ZnO@C and In_2O_3 NPs achieve the highest FE_{HCOO^-} values of 34% at −1.1 V and 53% at −1.3 V, respectively (Fig. S21, ESI†). The metal-free carbon nanocube sample exhibits a poor catalytic performance for the CO_2RR, and the main product is H_2 (Fig. S22, ESI†). A detailed comparison with various electrocatalysts in the literature is shown in Table S1 (ESI†).

Based on our experimental results and literature results on CO_2 reduction to formate,[6,13] a pathway for CO_2 reduction at In/ZnO@C is shown in eqn (1)–(5). In the equations, the label * denotes a free catalytic site.

$$CO_2\ (solution) + * \rightarrow *CO_2 \quad (1)$$

$$*CO_2 + e^- \rightarrow *CO_2^- \quad (2)$$

$$*CO_2^- + HCO_3^- \rightarrow HCOO* + CO_3^{2-} \quad (3)$$

$$HCOO* + e^- + HCO_3^- \rightarrow HCOOH* + CO_3^{2-} \quad (4)$$

$$HCOOH* \rightarrow HCOO^-\ (solution) + H^+ + * \quad (5)$$

Apart from the electrocatalytic activity, stability is also a significant parameter of electrocatalysts for practical applications. In Fig. S23 (ESI†), no evident decay in the current density is observed during long-term electrolysis for 12 h, demonstrating the remarkable stability of the as-prepared In/ZnO@C. The SEM image (Fig. S24, ESI†) and XRD pattern (Fig. S25, ESI†) confirm that the morphology and structure of the nanocubes are maintained well after the electrolysis test.

In order to clearly evaluate the specific catalytic performance of $HCOO^-$ during the CO_2RR, the $HCOO^-$ partial current densities of the as-prepared electrocatalysts were calculated at various potentials (Fig. 3C). It is apparent that In/ZnO@C exhibits the highest j_{HCOO^-} value at all applied potentials relative to the other samples, reaching a partial current density of 23.5 mA cm^{-2} at −1.2 V. This value is nearly 5 and 11.6 times higher than that of ZnO@C (4.7 mA cm^{-2}) and In_2O_3 NPs (2.0 mA cm^{-2}), respectively. Tafel plots based on the partial current density for $HCOO^-$ production were also constructed to understand the reaction kinetics of CO_2 reduction, showing a slope of 246 mV dec^{-1} for In/ZnO@C, which is smaller than that for ZnO@C (396 mV dec^{-1}) and In_2O_3 NPs (297 mV dec^{-1}) (Fig. 3D). The interfacial charge-transfer kinetics of the as-prepared catalysts were analyzed by electrochemical impedance spectroscopy (EIS). In Fig. S26 (ESI†), the diameters of the semicircles in the Nyquist plots confirm that In/ZnO@C possesses the smallest charge-transfer resistance (R_{ct}), which is consistent with the Tafel slope results.

The electrochemically active surface area (ECSA) value was evaluated by calculating the double layer capacitance (C_{dl}) to evaluate the active site numbers. The values of C_{dl} can be determined by CVs at various rates in the CO_2-saturated electrolyte (Fig. S27, ESI†), which are 1.2 mF cm^{-2} for In/ZnO@C and 0.56 mF cm^{-2} for the In_2O_3 NPs. These demonstrate that In/ZnO@C possesses the larger ECSA and rich active sites,

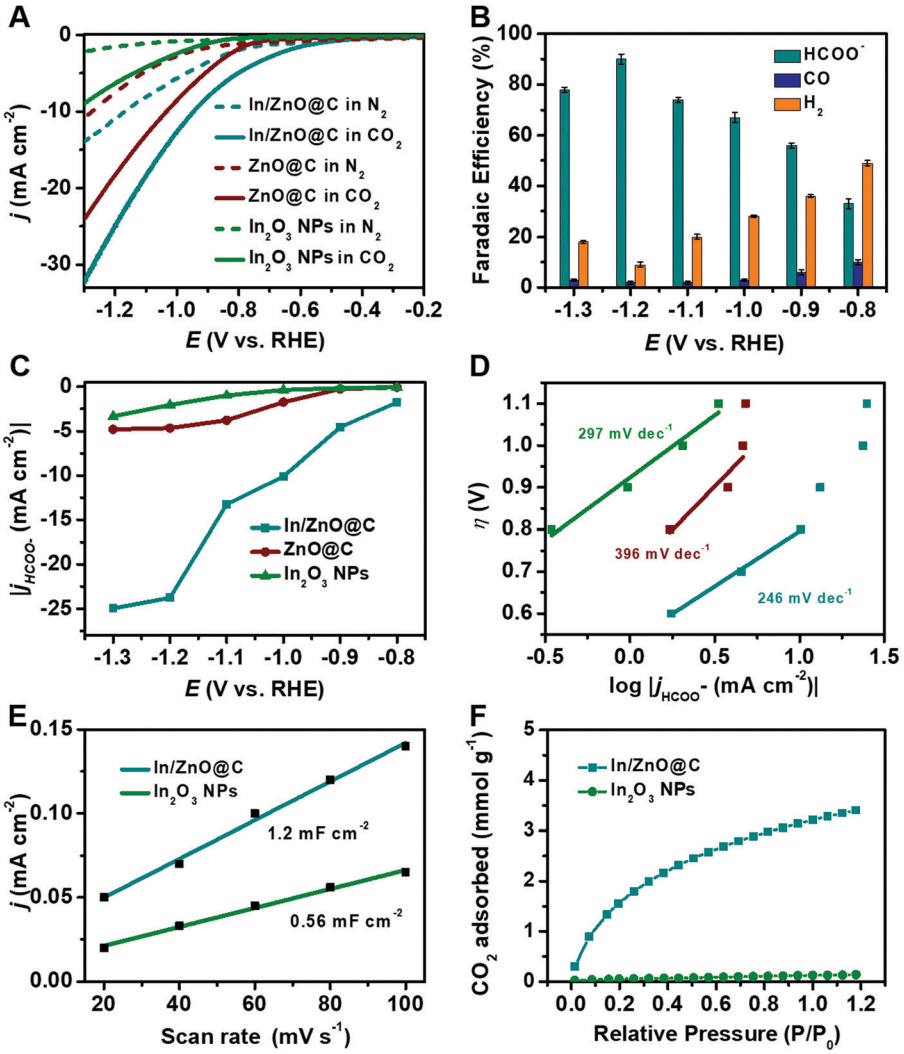

Fig. 3 (A) LSV curves in N_2- and CO_2-saturated 0.5 M $KHCO_3$ solutions for In/ZnO@C, ZnO@C and In_2O_3 NPs. (B) Variation in FE_{HCOO^-}, FE_{CO} and FE_{H2} for In/ZnO@C with the applied potential. (C) Potential-dependent, partial current densities for $HCOO^-$ formation for In/ZnO@C, ZnO@C and In_2O_3 NPs in CO_2-saturated 0.5 M $KHCO_3$ solutions. (D) Tafel plots (overpotential *vs.* $\log(|j_{HCOO^-}|)$) for In/ZnO@C, ZnO@C and In_2O_3 NPs. (E) Capacitive current densities, Δj, at a potential of 0.25 V *vs.* RHE plotted against the scan rate; a linear regression analysis gave the value for C_{dl}. (F) CO_2 adsorption isotherms for In/ZnO@C and In_2O_3 NPs.

consistent with the above morphology characterization. The surface area and porous properties of the as-prepared catalyst were further analyzed by N_2 adsorption and desorption measurements. As shown in Fig. S28 (ESI†), the typical type-IV isotherm curve with an apparent hysteresis loop under the N_2 pressure (P/P_0 = 0.5–1.0) region confirms the presence of abundant mesopores of In/ZnO@C.[31,47] The obtained Brunauer–Emmett–Teller (BET) surface area of In/ZnO@C is 171.53 $m^2\ g^{-1}$, and the corresponding pore size distribution curve reveals a main pore size of 3.5–4 nm. By contrast, the BET surface area of In_2O_3 NPs is only 13.73 $m^2\ g^{-1}$. The high surface area with mesopores is favorable for the exposure of more active surface sites for electrochemical reactions. CO_2 adsorption isotherms (Fig. 3F) show that In/ZnO@C has a much higher adsorption capacity (3.2 mmol g^{-1}) than In_2O_3 NPs (0.12 mmol g^{-1}) at P/P_0 = 1.0, which also contributes to the enhanced CO_2RR performance of In/ZnO@C.

Overall CO_2/H_2O splitting

An electrochemical CO_2 reduction system is composed of an anode and a cathode separated by a proton-exchange membrane with an electrolyte containing dissolved CO_2, as shown in Fig. 4A. The cathode supplies the catalytic active sites for the electrochemical CO_2RR, and the anode promotes oxidation reactions, *e.g.*, the oxygen evolution reaction (OER). The membrane separates the oxidation products from the reduction products while allowing the exchange of protons (H^+) to maintain the charge balance. Obviously, the CO_2RR at the electrocatalyst is the most crucial process for the overall electrochemical CO_2 reduction system. Inspired by the CO_2RR performance of In/ZnO@C, a CO_2RR–OER full cell was constructed by coupling the In/ZnO@C electrode as the cathode and a RuO_2/Ti electrode as the anode.

The RuO_2/Ti electrode used here was first evaluated by LSV using the three-electrode setup. As shown in Fig. 4B, the anodic OER current starts at 1.5 V and reaches 10 mA cm^{-2} at 1.88 V in

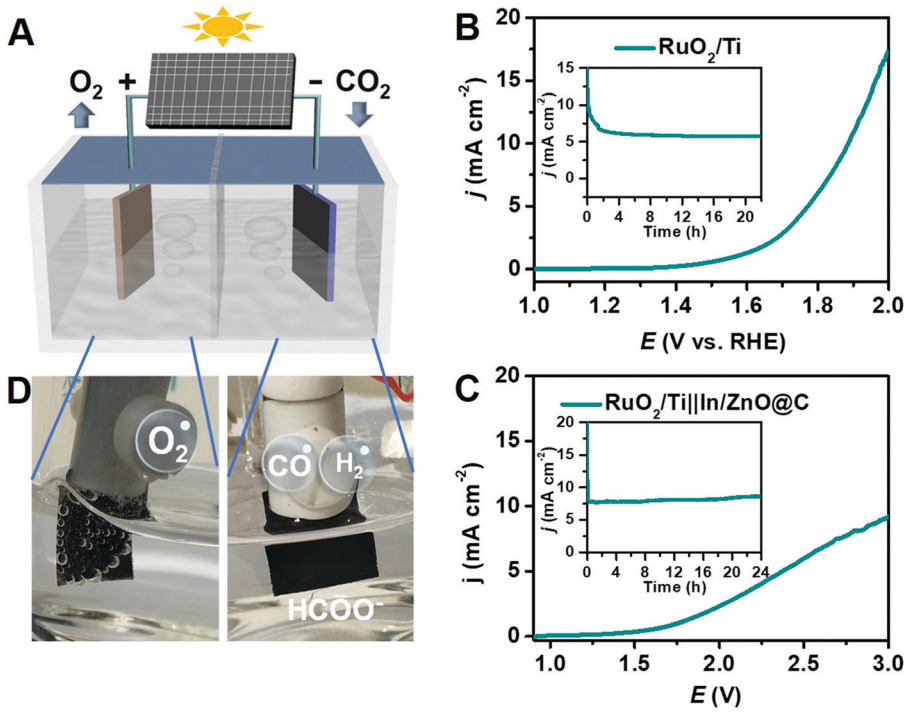

Fig. 4 (A) Schematic illustration of the CO_2RR–OER full cell. (B) OER polarization curve and electrolysis curve at 1.8 V for RuO_2/Ti in 0.5 M $KHCO_3$. (C) CO_2RR–OER polarization curve and electrolysis curve with an applied cell voltage of 2.7 V for the full cell. (D) Digital images showing the bubbles on two electrodes during solar-driven CO_2RR–OER electrolysis.

0.5 M $KHCO_3$. During long-term electrolysis at 1.8 V, the electrode shows a sustained current density of ~5.5 mA cm^{-2}. A polarization curve for the two-electrode full cell, RuO_2/Ti||In/ZnO@C, is presented in Fig. 4C. The coupled reactions deliver a current density of ~1 mA cm^{-2} at 1.78 V. The long-term electrolysis conducted at 2.7 V gives a stable current density of ~8 mA cm^{-2} without obvious degradation over the electrolysis period. The average yield of formate (FE_{HCOO^-}) is ~62% under the full-cell electrolysis conditions.

The electrolyzer was extended to a commercial Si solar cell with an output voltage of ~3 V. With natural sunlight as the light source, vigorous O_2 bubble formation was observed on the RuO_2/Ti electrode, while CO/H_2 bubbles were hardly visible on the In/ZnO@C electrode (Fig. 4D), consistent with the selective reduction of CO_2 to formate. The result points to a combined RuO_2/Ti||In/ZnO@C solar cell as a possible approach to a sustainable, renewable energy source for solar formate production.

Aqueous rechargeable Zn–CO_2 batteries

Considering the high CO_2RR performance of In/ZnO@C hollow nanocubes, an aqueous Zn–CO_2 battery was designed as shown in Fig. 5A. The catholyte and anolyte were CO_2-saturated 0.8 M $KHCO_3$ and 0.8 M KOH with 0.02 M $Zn(Ac)_2$, respectively, and the bipolar membrane was used to maintain the different pH values of the two compartments.[48] During the discharge process, the cathodic CO_2RR occurred driven by the dissolution of Zn foil to Zn^{2+} on the anode. During the charge process with energy input, the reaction of Zn deposition occurred on the anode, and the OER took place on the cathode.[49,50] Fig. 5B provides the OER performance and stability of the In/ZnO@C electrode. As shown in Fig. 5C, the charge–discharge voltage profile of the Zn–CO_2 battery with In/ZnO@C as the cathode confirms the rechargeable feature of the battery. As expected, the gap between charge–discharge polarization voltages increases with the increase of the current density. Besides, the Zn–CO_2 battery delivered a peak power density of 1.32 mW cm^{-2} at 0.32 V, along with an achieved current density of 4.2 mA cm^{-2} during the discharge process in the inset.

In Fig. 5D, the open-circuit voltage (OCV) was also measured using a voltammeter, and the displayed value (1.35 V) is consistent with that determined from the charge–discharge polarization curves. Fig. 5E confirms that the battery having the OCV can launch an electronic clock, demonstrating the effective energy output of the Zn–CO_2 battery. In Fig. 5F, the galvanostatic discharge was performed at various current densities, which reveal stable voltage plateaus for the Zn–CO_2 battery. Specifically, at a discharge current density of 7 mA cm^{-2}, the FE_{HCOO^-} is determined to be ~57%. When the Zn–CO_2 battery is cycled at a constant current density of 1 mA cm^{-2} (Fig. 5G), the battery delivers a discharge voltage of 0.6 V with an energy density of 495 Wh kg^{-1} (C_{Zn}: 824.5 mAh g^{-1}) and a charge voltage of 2.2 V, corresponding to a discharge–charge voltage gap of 1.6 V. The voltage gap is nearly unchanged after being cycled over 51 h (153 cycles), demonstrating the high durability of the Zn–CO_2 battery. In Table S2 (ESI†), the comparison of the performance of Zn–CO_2 batteries demonstrates that the rechargeable behavior of In/ZnO@C is competitive with other CO_2 reduction cathodes in the literature.

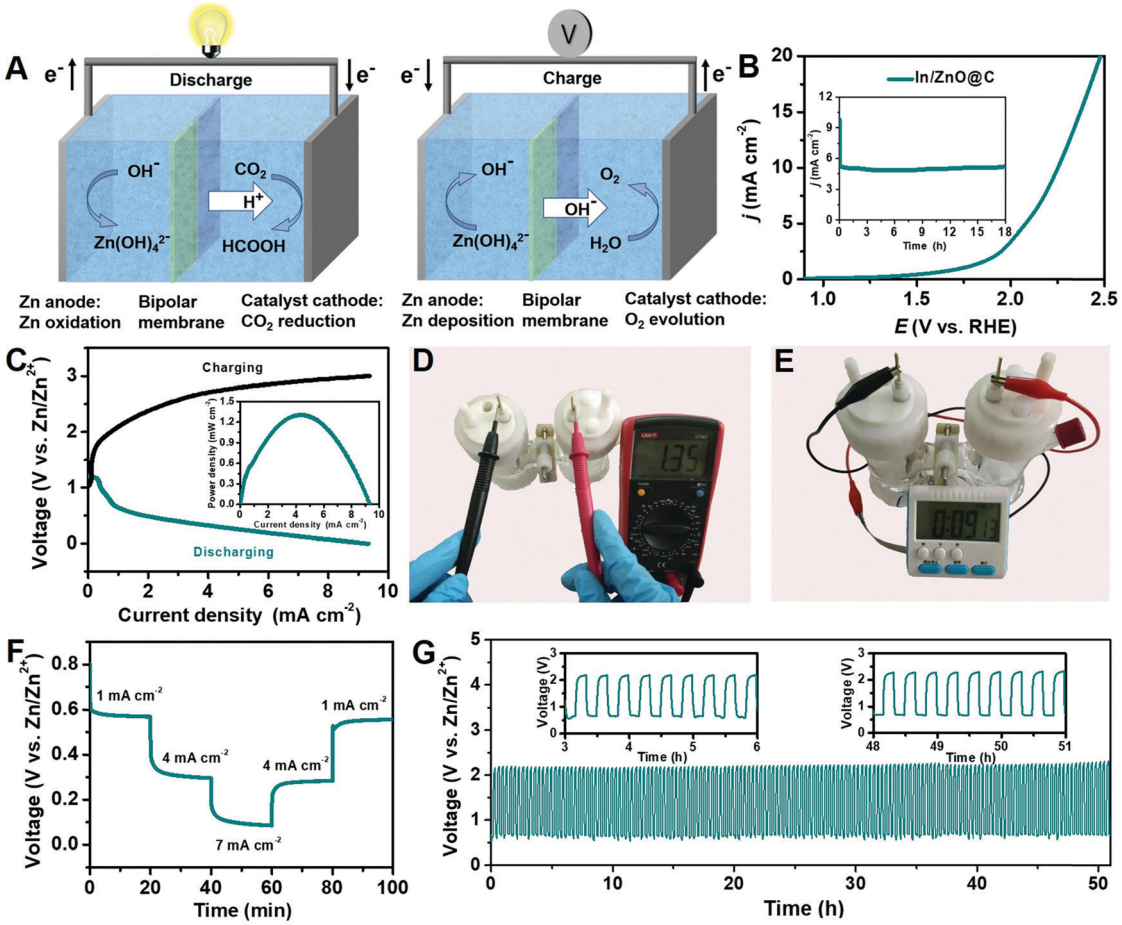

Fig. 5 (A) Schematic illustration of the aqueous Zn–CO_2 battery with the In/ZnO@C cathode. During the discharge process, Zn anode dissolution provides the driving force for CO_2 reduction on the cathode. During the charge process, Zn deposits on the anode and O_2 forms on the cathode with energy input. (B) O_2 evolution LSV curve of In/ZnO@C in 0.5 M $KHCO_3$. (C) Charge–discharge polarization curves and the power density curve of the Zn–CO_2 battery shown in the inset. (D) Digital image of the assembled Zn–CO_2 battery exhibiting a maximum open-circuit voltage of 1.35 V measured using a voltammeter. (E) Digital image of the electronic clock launched by the Zn–CO_2 battery with the In/ZnO@C cathode. (F) Galvanostatic discharge curves at various current densities. (G) Galvanostatic discharge–charge cycling curves at 1 mA cm^{-2}; the insets are magnified discharge–charge cycles at the initial and final times.

Conclusions

In summary, we have successfully synthesized In/ZnO@C hollow nanocubes with N-doped carbon as a support derived from $In(OH)_3$-doped Zn-MOF solid nanocubes. The resultant In/ZnO@C takes advantages of Zn-MOF as the unique nanocube matrix and metallic In as the active component, and the formation of the hollow nanostructure is associated with the carbothermal reduction reaction between $In(OH)_3$ and Zn-MOF. In/ZnO@C exhibits a remarkable activity and selectivity for CO_2 reduction to formate, reaching a partial current density of 23.5 mA cm^{-2} with a Faradaic efficiency of 90% at a potential of −1.2 V *vs.* RHE. Moreover, the electrocatalyst maintains remarkable stability with negligible changes in the hollow nanocube structure during long-term electrolysis. When the performance of the In/ZnO@C electrode was integrated with a home-made RuO_2/Ti electrode for water oxidation, CO_2RR–OER electrolysis was successfully driven by the solar cell as a renewable energy source for an extended period of time. Furthermore, an aqueous rechargeable Zn–CO_2 battery with In/ZnO@C as the cathode and Zn foil as the anode was constructed. It has an open-circuit voltage of 1.35 V and can deliver a peak power density of 1.32 mW cm^{-2} with the simultaneous conversion of CO_2 to formate. This study opens up an appealing approach to design a highly active and selective electrocatalyst for CO_2 reduction with a unique morphology and tunable composition.

Conflicts of interest

There are no conflicts to declare.

Acknowledgements

This work was supported by the National Natural Science Foundation of China (21872105 and 22072107) and the Science and Technology Commission of Shanghai Municipality (19DZ2271500).

References

1 D. T. Whipple and P. J. A. Kenis, Prospects of CO_2 utilization *via* direct heterogeneous electrochemical reduction, *J. Phys. Chem. Lett.*, 2010, **1**, 3451–3458.

2 J. P. Jones, G. K. S. Prakash and G. A. Olah, Electrochemical CO_2 reduction: recent advances and current trends, *Isr. J. Chem.*, 2014, **54**, 1451–1466.

3 R. Kortlever, J. Shen, K. J. Schouten, F. Calle-Vallejo and M. T. Koper, Catalysts and reaction pathways for the electrochemical reduction of carbon dioxide, *J. Phys. Chem. Lett.*, 2015, **6**, 4073–4082.

4 Y. Yan, L. Ke, Y. Ding, Y. Zhang, K. Rui, H. Lin and J. Zhu, Recent advances in Cu-based catalysts for electroreduction of carbon dioxide, *Mater. Chem. Front*, 2021, **5**, 2668–2683.

5 A. D. Handoko, F. Wei, Jenndy, B. S. Yeo and Z. W. Seh, Understanding heterogeneous electrocatalytic carbon dioxide reduction through operando techniques, *Nat. Catal.*, 2018, **1**, 922–934.

6 C. Long, X. Li, J. Guo, Y. Shi, S. Liu and Z. Tang, Electrochemical reduction of CO_2 over heterogeneous catalysts in aqueous solution: recent progress and perspectives, *Small Methods*, 2018, **3**, 1800369.

7 H. B. Yang, S.-F. Hung, S. Liu, K. Yuan, S. Miao, L. Zhang, X. Huang, H.-Y. Wang, W. Cai, R. Chen, J. Gao, X. Yang, W. Chen, Y. Huang, H. M. Chen, C. M. Li, T. Zhang and B. Liu, Atomically dispersed Ni(I) as the active site for electrochemical CO_2 reduction, *Nat. Energy*, 2018, **3**, 140–147.

8 S. Verma, B. Kim, H. R. Jhong, S. Ma and P. J. Kenis, A gross-margin model for defining technoeconomic benchmarks in the electroreduction of CO_2, *ChemSusChem*, 2016, **9**, 1972–1979.

9 Y.-J. Zhang, V. Sethuraman, R. Michalsky and A. A. Peterson, Competition between CO_2 Reduction and H_2 Evolution on Transition-Metal Electrocatalysts, *ACS Catal.*, 2014, **4**, 3742–3748.

10 C. Yang, J. Chai, Z. Wang, Y. Xing, J. Peng and Q. Yan, Recent progress on bismuth-based nanomaterials for electrocatalytic carbon dioxide reduction, *Chem. Res. Chin. Univ.*, 2020, **36**, 410–419.

11 Y. Hori, Electrochemical CO_2 reduction on metal electrodes, *Mod. Aspects Electrochem.*, 2008, **42**, 89–189.

12 W. Luo, W. Xie, M. Li, J. Zhang and A. Züttel, 3D hierarchical porous indium catalyst for highly efficient electroreduction of CO_2, *J. Mater. Chem. A*, 2019, **7**, 4505–4515.

13 N. Han, P. Ding, L. He, Y. Li and Y. Li, Promises of main group metal-based nanostructured materials for electrochemical CO_2 reduction to formate, *Adv. Energy Mater.*, 2019, **10**, 1902338.

14 Z. M. Detweiler, J. L. White, S. L. Bernasek and A. B. Bocarsly, Anodized indium metal electrodes for enhanced carbon dioxide reduction in aqueous electrolyte, *Langmuir*, 2014, **30**, 7593–7600.

15 Z. Bitar, A. Fecant, E. Trela-Baudot, S. Chardon-Noblat and D. Pasquier, Electrocatalytic reduction of carbon dioxide on indium coated gas diffusion electrodes—Comparison with indium foil, *Appl. Catal., B*, 2016, **189**, 172–180.

16 D. Farrusseng, S. Aguado and C. Pinel, Metal-organic frameworks: opportunities for catalysis, *Angew. Chem., Int. Ed.*, 2009, **48**, 7502–7513.

17 A. Corma, H. Garcia and F. X. Llabres, i Xamena, Engineering metal organic frameworks for heterogeneous catalysis, *Chem. Rev.*, 2010, **110**, 4606–4655.

18 J. Wen, Y. Li and J. Gao, Two-dimensional metal-organic frameworks and derivatives for electrocatalysis, *Chem. Res. Chin. Univ.*, 2020, **36**, 662–679.

19 Y. V. Kaneti, J. Tang, R. R. Salunkhe, X. Jiang, A. Yu, K. C. Wu and Y. Yamauchi, Nanoarchitectured design of porous materials and nanocomposites from metal-organic frameworks, *Adv. Mater.*, 2017, **29**, 1604898.

20 Z. Wang, N. Yang and D. Wang, When hollow multishelled structures (HoMSs) meet metal-organic frameworks (MOFs), *Chem. Sci.*, 2020, **11**, 5359–5368.

21 M. Liu, M. Yang, X. Shu and J. Zhang, Design strategies for carbon-based electrocatalysts and application to oxygen reduction in fuel cells, *Acta Phys.-Chim. Sin.*, 2020, **37**, 2007072.

22 Y. Y. Birdja, R. E. Vos, T. A. Wezendonk, L. Jiang, F. Kapteijn and M. T. M. Koper, Effects of substrate and polymer encapsulation on CO_2 electroreduction by immobilized indium(III) protoporphyrin, *ACS Catal.*, 2018, **8**, 4420–4428.

23 R. Hegner, L. F. M. Rosa and F. Harnisch, Electrochemical CO_2 reduction to formate at indium electrodes with high efficiency and selectivity in pH neutral electrolytes, *Appl. Catal., B*, 2018, **238**, 546–556.

24 Z. Zhang, F. Ahmad, W. Zhao, W. Yan, W. Zhang, H. Huang, C. Ma and J. Zeng, Enhanced electrocatalytic reduction of CO_2 *via* chemical coupling between indium oxide and reduced graphene oxide, *Nano Lett.*, 2019, **19**, 4029–4034.

25 L. Yu, H. Hu, H. B. Wu and X. W. Lou, Complex hollow nanostructures: synthesis and energy-related applications, *Adv. Mater.*, 2017, **29**, 1604563.

26 Q. Qian, Y. Li, Y. Liu and G. Zhang, General anion-exchange reaction derived amorphous mixed-metal oxides hollow nanoprisms for highly efficient water oxidation electrocatalysis, *Appl. Catal., B*, 2020, **266**, 118642.

27 F. You, J. Wan, J. Qi, D. Mao, N. Yang, Q. Zhang, L. Gu and D. Wang, Lattice distortion in hollow multi-shelled structures for efficient visible-light CO_2 reduction with a SnS_2/SnO_2 junction, *Angew. Chem., Int. Ed.*, 2020, **59**, 721–724.

28 Z. Zhang, G. Wen, D. Luo, B. Ren, Y. Zhu, R. Gao, H. Dou, G. Sun, M. Feng, Z. Bai, A. Yu and Z. Chen, "Two ships in a bottle" design for Zn–Ag–O catalyst enabling selective and long-lasting CO_2 electroreduction, *J. Am. Chem. Soc.*, 2021, **143**, 6855–6864.

29 T. Wang, X. Sang, W. Zheng, B. Yang, S. Yao, C. Lei, Z. Li, Q. He, J. Lu, L. Lei, L. Dai and Y. Hou, Gas diffusion strategy for inserting atomic iron sites into graphitized carbon supports for unusually high-efficient CO_2 electroreduction and high-performance Zn–CO_2 batteries, *Adv. Mater.*, 2020, **32**, 2002430.

30 J. Xie, Z. Zhou and Y. Wang, Metal–CO_2 batteries at the crossroad to practical energy storage and CO_2 recycle, *Adv. Funct. Mater.*, 2019, **30**, 1908285.

31 Y. Niu, X. Teng, S. Gong and Z. Chen, A bimetallic alloy anchored on biomass-derived porous N-doped carbon fibers as a self-supporting bifunctional oxygen electrocatalyst for flexible Zn–air batteries, *J. Mater. Chem. A*, 2020, **8**, 13725–13734.

32 X. Shu, S. Chen, S. Chen, W. Pan and J. Zhang, Cobalt nitride embedded holey N-doped graphene as advanced bifunctional electrocatalysts for Zn-air batteries and overall water splitting, *Carbon*, 2020, **157**, 234–243.

33 K. S. Park, Z. Ni, A. P. Cote, J. Y. Choi, R. Huang, F. J. Uribe-Romo, H. K. Chae, M. O'Keeffe and O. M. Yaghi, Exceptional chemical and thermal stability of zeolitic imidazolate frameworks, *Proc. Natl. Acad. Sci. U. S. A.*, 2006, **103**, 10186–10191.

34 S. Gadipelli, Z. Li, T. Zhao, Y. Yang, T. Yildirim and Z. Guo, Graphitic nanostructures in a porous carbon framework significantly enhance electrocatalytic oxygen evolution, *J. Mater. Chem. A*, 2017, **5**, 24686–24694.

35 P. Lu, X. Tan, H. Zhao, Q. Xiang, K. Liu, X. Zhao, X. Yin, X. Li, X. Hai, S. Xi, A. T. S. Wee, S. J. Pennycook, X. Yu, M. Yuan, J. Wu, G. Zhang, S. C. Smith and Z. Yin, Atomically dispersed indium sites for selective CO_2 electroreduction to formic acid, *ACS Nano*, 2021, **15**, 5671–5678.

36 W. Zhang, Z. Yue, Q. Wang, X. Zeng, C. Fu, Q. Li, X. Li, L. Fang and L. Li, Carbon-encapsulated CoS_2 nanoparticles anchored on N-doped carbon nanofibers derived from ZIF-8/ZIF-67 as anode for sodium-ion batteries, *Chem. Eng. J.*, 2020, **380**, 122548.

37 X. Wang, X. Huang, W. Gao, Y. Tang, P. Jiang, K. Lan, R. Yang, B. Wang and R. Li, Metal–organic framework derived $CoTe_2$ encapsulated in nitrogen-doped carbon nanotube frameworks: a high-efficiency bifunctional electrocatalyst for overall water splitting, *J. Mater. Chem. A*, 2018, **6**, 3684–3691.

38 I. S. Amiinu, X. Liu, Z. Pu, W. Li, Q. Li, J. Zhang, H. Tang, H. Zhang and S. Mu, From 3D ZIF nanocrystals to Co-N_x/C nanorod array electrocatalysts for ORR, OER, and Zn–air batteries, *Adv. Funct. Mater.*, 2018, **28**, 1704638.

39 S. Zhang, L. Qiu, Y. Zheng, Q. Shi, T. Zhou, V. Sencadas, Y. Xu, S. Zhang, L. Zhang, C. Zhang, C. L. Zhang, S. H. Yu and Z. Guo, Rational design of core–shell ZnTe@N-doped carbon nanowires for high gravimetric and volumetric alkali metal ion storage, *Adv. Funct. Mater.*, 2020, **31**, 2006425.

40 W. Zhang, X. Jiang, X. Wang, Y. V. Kaneti, Y. Chen, J. Liu, J.-S. Jiang, Y. Yamauchi and M. Hu, Spontaneous weaving of graphitic carbon networks synthesized by pyrolysis of ZIF-67 crystals, *Angew. Chem., Int. Ed.*, 2017, **56**, 8435–8440.

41 M. Huang, K. Mi, J. Zhang, H. Liu, T. Yu, A. Yuan, Q. Kong and S. Xiong, MOF-derived Bi-metal embedded N-doped carbon polyhedral nanocages with enhanced lithium storage, *J. Mater. Chem. A*, 2017, **5**, 266–274.

42 Z. Geng, X. Kong, W. Chen, H. Su, Y. Liu, F. Cai, G. Wang and J. Zeng, Oxygen vacancies in ZnO nanosheets enhance CO_2 electrochemical reduction to CO, *Angew. Chem., Int. Ed.*, 2018, **57**, 6054–6059.

43 J. Lv, X. Yang, K. Li, X. Chen, S. Sun, H.-Y. Zang, Y.-F. Chang, Y.-H. Wang and Y.-G. Li, Introduction of Mn(III) to regulate the electronic structure of fluorine-doped nickel hydroxide for efficient water oxidation, *Nanoscale Adv.*, 2019, **1**, 4099–4108.

44 F. Lü, H. Bao, F. He, G. Qi, J. Sun, S. Zhang, L. Zhuo, H. Yang, G. Hu, J. Luo and X. Liu, Nitrogen dopant induced highly selective CO_2 reduction over lotus-leaf shaped ZnO nanorods, *Mater. Chem. Front.*, 2021, **5**, 4225–4230.

45 J. Wang, C. Liu, J. Feng, D. Cheng, C. Zhang, Y. Yao, Z. Gu, W. Hu, J. Wan and C. Yu, MOFs derived Co/Cu bimetallic nanoparticles embedded in graphitized carbon nanocubes as efficient Fenton catalysts, *J. Hazard. Mater.*, 2020, **394**, 122567.

46 J. L. DiMeglio and J. Rosenthal, Selective conversion of CO_2 to CO with high efficiency using an inexpensive bismuth-based electrocatalyst, *J. Am. Chem. Soc.*, 2013, **135**, 8798–8801.

47 X. Peng, L. Zhang, Z. Chen, L. Zhong, D. Zhao, X. Chi, X. Zhao, L. Li, X. Lu, K. Leng, C. Liu, W. Liu, W. Tang and K. P. Loh, Hierarchically porous carbon plates derived from wood as bifunctional ORR/OER electrodes, *Adv. Mater.*, 2019, **31**, 1900341.

48 F. Urbain, P. Tang, N. M. Carretero, T. Andreu, L. G. Gerling, C. Voz, J. Arbiol and J. R. Morante, A prototype reactor for highly selective solar-driven CO_2 reduction to synthesis gas using nanosized earth-abundant catalysts and silicon photovoltaics, *Energy Environ. Sci.*, 2017, **10**, 2256–2266.

49 X. Wang, J. Xie, M. A. Ghausi, J. Lv, Y. Huang, M. Wu, Y. Wang and J. Yao, Rechargeable Zn–CO_2 electrochemical cells mimicking two-step photosynthesis, *Adv. Mater.*, 2019, **31**, 1807807.

50 R. Yang, J. Xie, Q. Liu, Y. Huang, J. Lv, M. A. Ghausi, X. Wang, Z. Peng, M. Wu and Y. Wang, A trifunctional Ni–N/P–O-codoped graphene electrocatalyst enables dual-model rechargeable Zn–CO_2/Zn–O_2 batteries, *J. Mater. Chem. A*, 2019, **7**, 2575–2580.